

A simulation study on superparamagnetic nanoparticle based multi-tracer tracking

Kai Wu, Akash Batra, Shray Jain, Clark Ye, Jinming Liu, and Jian-Ping Wang

Citation: *Appl. Phys. Lett.* **107**, 173701 (2015);

View online: <https://doi.org/10.1063/1.4934743>

View Table of Contents: <http://aip.scitation.org/toc/apl/107/17>

Published by the [American Institute of Physics](#)

Articles you may be interested in

[Superparamagnetic nanoparticle-based viscosity test](#)

Applied Physics Letters **107**, 053701 (2015); 10.1063/1.4928057

[Real-time measurement of Brownian relaxation of magnetic nanoparticles by a mixing-frequency method](#)

Applied Physics Letters **98**, 213702 (2011); 10.1063/1.3595273

[Magnetic hyperthermia performance of magnetite nanoparticle assemblies under different driving fields](#)

AIP Advances **7**, 056327 (2017); 10.1063/1.4978458

[Magnetic properties of cubic FeCo nanoparticles with anisotropic long chain structure](#)

AIP Advances **6**, 056126 (2016); 10.1063/1.4945042

[Planar Hall effect sensor for magnetic micro- and nanobead detection](#)

Applied Physics Letters **84**, 4729 (2004); 10.1063/1.1759380

[Giant voltage manipulation of MgO-based magnetic tunnel junctions via localized anisotropic strain: A potential pathway to ultra-energy-efficient memory technology](#)

Applied Physics Letters **109**, 092403 (2016); 10.1063/1.4961670



Scilight

Sharp, quick summaries **illuminating**
the latest physics research

Sign up for **FREE!**

AIP
Publishing

A simulation study on superparamagnetic nanoparticle based multi-tracer tracking

Kai Wu,¹ Akash Batra,² Shray Jain,¹ Clark Ye,¹ Jinming Liu,¹ and Jian-Ping Wang^{1,a)}

¹Department of Electrical Engineering, University of Minnesota, 200 Union Street SE, Minneapolis, Minnesota 55455, USA

²Department of Mechanical Engineering, University of Wisconsin-Madison, 1513 University Avenue, Madison, Wisconsin 53706, USA

(Received 7 September 2015; accepted 15 October 2015; published online 26 October 2015)

Superparamagnetic nanoparticles (MNPs) have been utilized in biomedical sensing, detection, therapeutics, and diagnostics due to their unique magnetic response under different driving fields. In this letter, we report a multi-tracer tracking method that uses different kinds of MNPs as magnetic tracers along with two alternating magnetic fields that can be potentially used to build magnetic-based flow cytometry. By applying two driving fields at frequency f_H and f_L to MNPs, the response signal is measured at the combinatorial frequencies such as $f_H \pm 2f_L$ (3rd harmonics), $f_H \pm 4f_L$ (5th harmonics), $f_H \pm 6f_L$ (7th harmonics), and so on. Each MNP has its own signature of phase and amplitude, and it is possible to differentiate individual MNPs in a mixture. We theoretically demonstrated colorizing up to 4-MNP tracers in one mixture with an error rate lower than 10%. The performance of multi-tracer imaging can be optimized by increasing the driving field frequency, choosing MNPs with higher saturation magnetization, and using MNP tracers with more centralized size distribution. © 2015 AIP Publishing LLC. [<http://dx.doi.org/10.1063/1.4934743>]

Currently, optical flow cytometry (FCM) has been widely used in clinics, biological studies, and research laboratories.¹ The increasing demand on polychromatic FCM for applications in complex immune systems has pushed the frontiers of FCM beyond 12-colour systems.² However, there is still a long way to go for FCM to become a point of care (POC) and easy-to-use device due to bulky size, high cost, and mechanical complexity.³

Superparamagnetic nanoparticles (MNPs) have been used in biological and medical^{4–6} applications for decades due to their comparable size to biomolecules such as proteins.^{7,8} One of the reasons in choosing MNPs for biological applications is their biocompatibility, nontoxicity, and high level of accumulation in target biological tissues.⁹ The most appealing feature of MNPs is their reaction to magnetic force. Furthermore, most biological systems show little (or no) ferromagnetism, diamagnetism, or paramagnetism properties, which means MNPs can be detected from biological samples with little background noise.^{10,11} Nowadays, MNPs can be readily functionalized with ligands, aptamers, and proteins¹² and thus can be bound to cells and biomolecules.¹³ Functionalized MNPs are one of the most promising candidates for applications in biolabeling.¹⁴ Not only the fluorophores but also MNPs can be used as tracers for colorization purposes.¹⁵ In this letter, we report an MNP based multi-tracer imaging method that can potentially be used to build magnetic polychromatic FCM. We theoretically demonstrated the feasibility of using a mixing frequency method^{16–18} to distinguish up to 4 types of MNPs in one suspension in one test with an error rate lower than 10%. The complete signal acquisition process was simulated. By

utilizing both the phase and the amplitude information of each type of MNP tracer at the 3rd, 5th, 7th, 9th, and 11th harmonics, we are able to estimate the number of each MNP tracer by knowing the phase and the amplitude of the MNP mixture.

We assumed a typical detection coil system with two driving field coils and one detection coil.^{17,19–23} Two alternating magnetic fields (AMFs) are applied to MNPs, one with low frequency f_L but high amplitude A_L , and the other with high frequency f_H but low amplitude A_H , expressed as $H(t) = A_H \sin(2\pi f_H t) + A_L \sin(2\pi f_L t)$. Typically, we assume that $f_H = 300$ kHz, $f_L = 500$ Hz, $A_H = 5$ Oe, and $A_L = 25$ Oe.

Five types of spherical MNPs with an average core diameter of 30 nm are assumed in this letter: Fe (saturation magnetization $M_s = 1700$ emu/cm³), FeCo ($M_s = 2300$ emu/cm³), FeCo/FeCoO ($M_s = 2000$ emu/cm³), Co ($M_s = 1100$ emu/cm³), and Fe₃O₄ ($M_s = 900$ emu/cm³). Magnetizations of these MNPs obey the Langevin function^{8,17–21,24,25}

$$M_D(t) = m_s c L(\xi) = m_s c \left(\coth \xi - \frac{1}{\xi} \right), \quad (1)$$

where $m_s = \frac{1}{6} \pi D^3 M_s$, $\xi = \frac{m_s \mu_0 H(t)}{k_B T}$, the concentration of MNPs is assumed to be $c = 0.17 \frac{\text{nmol}}{\text{ml}} = 10^{14}/\text{ml}$, L is the Langevin function, k_B is the Boltzmann constant, T is the absolute temperature, and μ_0 is the vacuum permeability. Magnetization curves of these MNPs following the Langevin function are plotted in Fig. 1.

The amplitude of the low frequency driving field A_L is high enough to get MNPs into the nonlinear region (Fig. 1), whereas the high frequency field modulates signals into the high frequency region where $1/f$ noise is lower. As a result, driving fields nonlinearly modulate the response signal.^{18,20}

^{a)} Author to whom correspondence should be addressed. Electronic mail: jpwang@umn.edu.

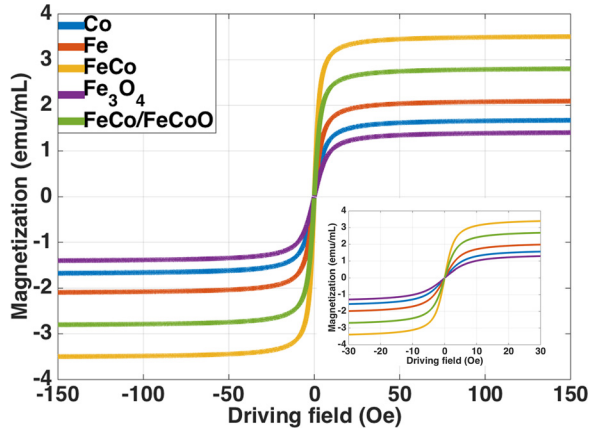


FIG. 1. Magnetization curve of each type of MNP.

The response signal contains a linear combination of $mf_H + nf_L$ where m and n are integers.^{17,20} Amplitudes and phases from the 3rd harmonics ($f_H \pm 2f_L$), 5th harmonics ($f_H \pm 4f_L$), and 7th harmonics ($f_H \pm 6f_L$) are utilized.

According to the Nyquist criterion, the sampling rate is set to be $f_s = 1$ MHz. Fig. 2(a) shows the real-time magnetization response of 3-MNP tracers under two alternating magnetic fields. The induced voltage (see Fig. 2(b)) is collected according to Lenz's law^{19,21}

$$u(t) = -N_w \mu_0 S_0 V \frac{d}{dt} M(t), \quad (2)$$

where the area of the detection coil is assumed to be $S_0 = \pi R^2 = \pi(2.5 \times 10^{-3} \text{ m})^2 = 2 \times 10^{-5} \text{ m}^2$, the number of windings N_w is assumed to be 1000, and V is the volume of the MNP solution.

By performing Fast Fourier Transform (FFT) on the discrete-time voltage signal, the spectra from the total mixture and from each type of MNPs are collected (Fig. 3). We added white noise and pink noise²³ into the signal to make it

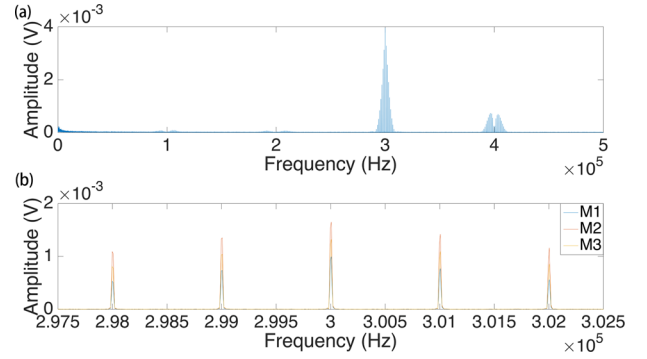


FIG. 3. Amplitude spectrum of (a) MNPs in total and (b) each type of MNP (3-MNP tracer imaging).

closer to real cases. The real-time magnetization, induced voltage from each type of MNPs, and the amplitude spectrum of 2-MNP, 4-MNP, and 5-MNP tracer imaging can be found from Ref. 23.

Each type of MNP tracers has its own signature of phase and amplitude and will respond independently to the driving fields. Thus, it is possible to identify a specific type of MNP tracer from another.²¹ The voltage of any one of the MNPs at a specific frequency is represented by a phasor whose amplitude, angular frequency, and phase are time-invariant.²¹ Thus, the phasor from a mixture of multi-MNP tracers is simply the weighed sum of multiple phasors. Take a typical 3-MNP tracer imaging system as an example. The amplitudes and phases from the 3rd and 5th harmonics of each type of MNP per unit volume are expressed as $A_{31}, \phi_{31}, A_{32}, \phi_{32}, A_{33}, \phi_{33}, A_{51}, \phi_{51}, A_{52}, \phi_{52}, A_{53},$ and ϕ_{53} , respectively. The 3rd and 5th harmonics amplitudes and phases from the MNP mixture are expressed as A_{3t}, ϕ_{3t} and A_{5t}, ϕ_{5t} . Three types of MNP tracers are mixed in different volume ratios. Assume that the number of MNP tracers are $a, b,$ and c times of the number per unit volume. Thus, the equation set based on phasor theory is expressed as

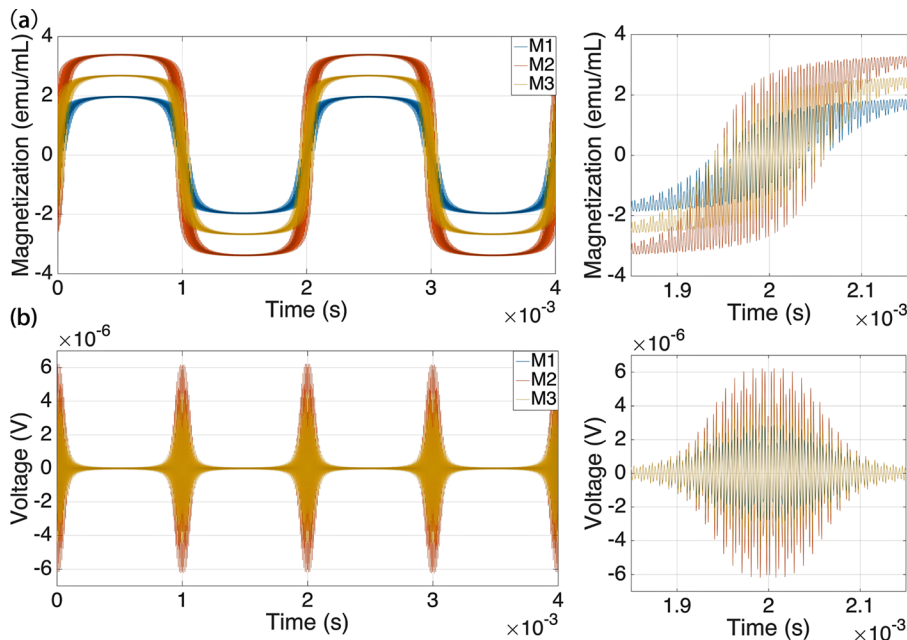


FIG. 2. (a) Real-time magnetization of each type of MNP. (b) Real-time voltage induced from each type of MNP (3-MNP tracer imaging).

$$\begin{cases} A_3 t \times \cos(\phi_3 t) = a \times A_3 1 \times \cos(\phi_3 1) + b \times A_3 2 \times \cos(\phi_3 2) + c \times A_3 3 \times \cos(\phi_3 3) \\ A_3 t \times \sin(\phi_3 t) = a \times A_3 1 \times \sin(\phi_3 1) + b \times A_3 2 \times \sin(\phi_3 2) + c \times A_3 3 \times \sin(\phi_3 3) \\ A_5 t \times \cos(\phi_5 t) = a \times A_5 1 \times \cos(\phi_5 1) + b \times A_5 2 \times \cos(\phi_5 2) + c \times A_5 3 \times \cos(\phi_5 3) \end{cases} \quad (3)$$

By solving the equation set above, the estimated volumes as well as the number of MNPs for each MNP tracer are derived. Error rates are calculated by comparing the estimated volumes of each MNP tracer and the real volumes in the mixture in order to assess the performance of the multi-tracer imaging.

We divided the magnetization curve in Fig. 1 into 3 regions: linear region I, nonlinear region II, and saturation region III²³ with applied driving field strength expressed as $H_I(t) = 5 \times \sin(2\pi f_H t) + 10 \times \sin(2\pi f_L t)$, $H_{II}(t) = 5 \times \sin(2\pi f_H t) + 25 \times \sin(2\pi f_L t)$, and $H_{III}(t) = 5 \times \sin(2\pi f_H t) + 100 \times \sin(2\pi f_L t)$, where $f_H = 300$ kHz, $f_L = 500$ Hz, and $A_H = 5$ Oe are identical.

The simulation is repeated 500 times in a 3-MNP tracer imaging system (the corresponding tracers are Fe, FeCo, and FeCo/FeCoO MNPs with identical diameters of 30 nm, mixed with a ratio of 2:3:5). The white and pink noises are randomized, thus making the error rate differ, in each run. The average error rates for each type of MNP in different regions are shown in Fig. 4(a). The error rate is higher than 100% when the driving field strength reaches the saturation region (region III). The calculated error rate on Fe reaches 10% in region I while the other two tracers are lower than 2% in region I. In region II, the error rate for all the MNP tracers is lower than 3%. We, therefore, conclude that multi-tracer imaging has better performance in region II.

The performance of multi-tracer imaging is largely dependent on the driving field—not only the field strength but also the field frequency. In a 3-MNP tracer imaging system,

we applied a driving field in region II: $H_{II}(t) = 5 \times \sin(2\pi f_H t) + 25 \times \sin(2\pi f_L t)$. We kept the amplitudes of the two driving fields constant and maintained the low frequency field at $f_L = 500$ Hz while sweeping the high frequency from 15 kHz to 400 kHz. As shown in Fig. 4(b), the overall trend of error rate decreases as the high frequency increases except for the data point at $f_H = 100$ kHz. This is because the noise floor (especially $1/f$ noise) is lower in higher frequency regions. Furthermore, according to Lenz's law (Equation (2)), MNPs under a fast changing field induce larger voltage in harmonics as well as larger phase lag after the field.

The driving field $H_{II}(t) = 5 \times \sin(2\pi f_H t) + 25 \times \sin(2\pi f_L t)$ with $f_H = 300$ kHz and $f_L = 500$ Hz is applied to MNP mixtures. Five types of MNP tracers with the volume ratio of Fe:FeCo: FeCo/FeCoO:Co:Fe₃O₄ = 2:3:5:7:9 are assumed. The 2-, 3-, 4-, and 5-MNP tracer imaging systems are simulated for 500 times, respectively. From Fig. 4(c), the error rate for all the tracers in the 4-MNP tracer imaging system is maintained at a rate lower than 10%, which means the multi-tracer imaging method works well on 4-MNP tracers. For the 5-MNP tracer imaging system, the error rate for imaging the number of tracer Fe from the mixture is high due to its relatively lower saturation magnetization M_s compared with FeCo, FeCo/FeCoO, and Co. Although Fe₃O₄ has lower M_s than Fe, its large volume ratio in the mixture lowers the error rate to nearly 10%. Thus, the multi-tracer imaging system works better for a large number of MNP tracers and MNPs with higher M_s .

The simulations above are based on an ideal case, namely, the MNPs have an identical size of 30 nm. In real

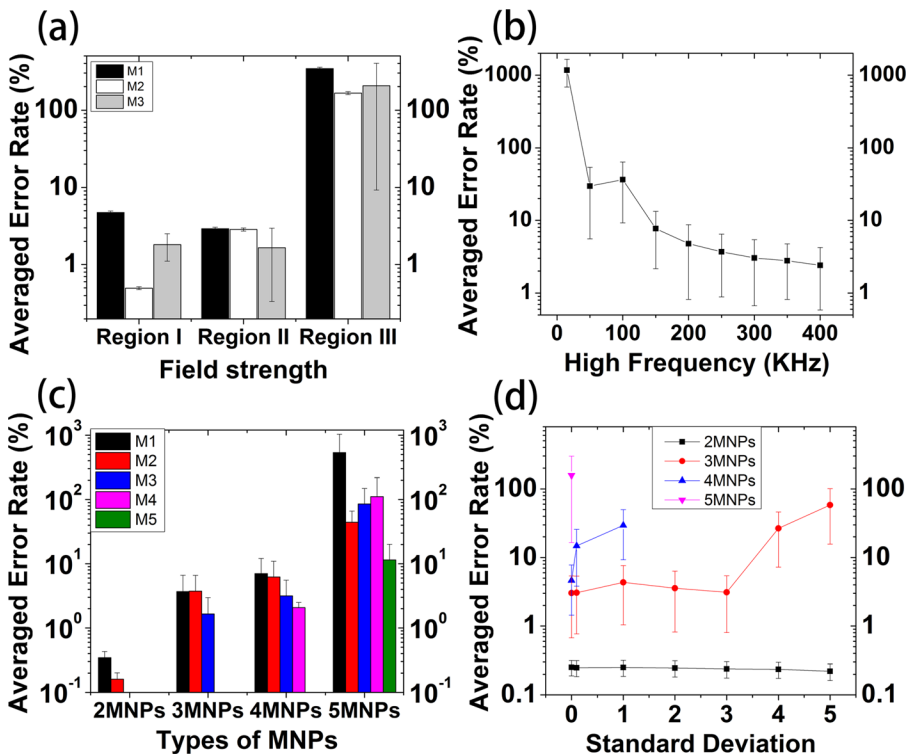


FIG. 4. (a) Error rate along field strength, (b) error rate vs. high frequency, (c) error rate along the number of MNP tracers, and (d) error rate vs. standard deviation.

cases, the size distribution of MNPs is described by the log-normal distribution, and it reduces to normal distribution when the size distribution is narrow.²⁶ Here, we assume MNPs with diameter D , which follows the normal distribution expressed as $D \sim N(30, \sigma)$ with an average core diameter of 30 nm and a standard deviation of σ ($\sigma = 0, 0.1, 1, 2, 3, 4, 5$) (size distribution histograms can be found from Ref. 23, $\sigma = 5$ means 68.3% of MNPs have diameters between 25 nm and 35 nm, and the rest are either smaller than 25 nm or larger than 35 nm). From Fig. 4(d), we found that for 2-MNP tracer imaging, the error rate is stable—lower than 0.3%. For 3-MNP tracer imaging, the error rate is lower than 5% as long as the standard deviation $\sigma \leq 3$. The error rate of 4-MNP tracer imaging is lower than 10% in the ideal case and around 15% when the standard deviation $\sigma = 0.1$.

In this letter, we reported a multi-tracer imaging method that is based on MNPs and the mixing-frequency method. Magnetic based multi-tracer colorization could potentially surpass fluorescence-based colorization in current FCM due to less or no magnetic background noise from biological samples, while fluorophores are more susceptible to the background noise.

We studied the multi-tracer imaging limit of this MNP based mixing-frequency method; the estimation error rate is lower than 10% for imaging up to 4 MNP tracers in one suspension. The performance of multi-tracer imaging benefits from MNPs with high saturation magnetizations. We also studied the best driving field strength where we can get a lower error rate. This MNP-based multi-tracer imaging method works well at the nonlinear region in the MH loop of MNPs. As we increase the frequencies of the driving field, the error rate decreases. Thus, a driving field with a higher frequency is preferred in order to get better performance in multi-tracer imaging. In real applications, diameters of MNPs follow normal distribution; in this letter, we also simulated MNPs with standard deviations, σ , varying from 0.1 to 5. Size variation has little effect on the error rate for the 2-MNP tracer imaging. The error rate for the 3-MNP tracer imaging increases when σ reaches or exceeds 4. For the 4-MNP tracer imaging, the error rate increases whenever there is a variation in size. However, when the standard deviation of MNPs is $\sigma = 0.1$, a still acceptable error rate of 15% is obtained.

The authors thank the support from the Institute of Engineering in Medicine, National Science Foundation MRSEC facility program, the Distinguished McKnight

University Professorship, UROP program, MNDrive STEM program, and the MNDrive program from the University of Minnesota.

- ¹R. R. Jahan-Tigh, C. Ryan, G. Obermoser, and K. Schwarzenberger, *J. Invest. Dermatol.* **132**(10), e1 (2012).
- ²S. P. Perfetto, P. K. Chattopadhyay, and M. Roederer, *Nat. Rev. Immunol.* **4**(8), 648–655 (2004).
- ³X. Mao, A. A. Nawaz, S.-C. S. Lin, M. I. Lapsley, Y. Zhao, J. P. McCoy, W. S. El-Deiry, and T. J. Huang, *Biomicrofluidics* **6**(2), 024113 (2012).
- ⁴L. Yu, J. Liu, K. Wu, T. Klein, Y. Jiang, and J.-P. Wang, *Sci. Rep.* **4**, 7216 (2014).
- ⁵Y. Wang, W. Wang, L. Yu, L. Tu, Y. Feng, T. Klein, and J.-P. Wang, *Biosens. Bioelectron.* **70**, 61–68 (2015).
- ⁶B. Gleich and J. Weizenecker, *Nature* **435**(7046), 1214–1217 (2005).
- ⁷C.-Y. Hong, C. Wu, Y. Chiu, S. Yang, H. Hornig, and H. Yang, *Appl. Phys. Lett.* **88**(21), 212512 (2006).
- ⁸A. M. Rauwerdink and J. B. Weaver, *Appl. Phys. Lett.* **96**(3), 033702 (2010).
- ⁹A. Ito, M. Shinkai, H. Honda, and T. Kobayashi, *J. Biosci. Bioeng.* **100**(1), 1–11 (2005).
- ¹⁰S.-H. Chung, A. Hoffmann, K. Gusliencko, S. Bader, C. Liu, B. Kay, L. Makowski, and L. Chen, *J. Appl. Phys.* **97**(10), 10R101 (2005).
- ¹¹X. Zhang, D. B. Reeves, I. M. Perreard, W. C. Kett, K. E. Griswold, B. Gimi, and J. B. Weaver, *Biosens. and Bioelectron.* **50**, 441–446 (2013).
- ¹²J. Zhou, C. Wang, P. Wang, P. B. Messersmith, and H. Duan, *Chem. Mater.* **27**(8), 3071–3076 (2015).
- ¹³D. Reich, M. Tanase, A. Hultgren, L. Bauer, C. Chen, and G. Meyer, *J. Appl. Phys.* **93**(10), 7275–7280 (2003).
- ¹⁴A. H. Lu, E. e., L. Salabas, and F. Schüth, *Angew. Chem. Int. Ed.* **46**(8), 1222–1244 (2007).
- ¹⁵L. Lenglet, *J. Magn. Magn. Mater.* **321**(10), 1639–1643 (2009).
- ¹⁶O. Cakmak, C. Elbuken, E. Ermeke, A. Mostafazadeh, I. Baris, B. Erdem Alaca, I. H. Kavakli, and H. Urey, *Methods* **63**(3), 225–232 (2013).
- ¹⁷H.-J. Krause, N. Wolters, Y. Zhang, A. Offenhäuser, P. Miethe, M. H. Meyer, M. Hartmann, and M. Keusgen, *J. Magn. Magn. Mater.* **311**(1), 436–444 (2007).
- ¹⁸K. Wu, J. Liu, Y. Wang, C. Ye, Y. Feng, and J.-P. Wang, *Appl. Phys. Lett.* **107**(5), 053701 (2015).
- ¹⁹K. Wu, Y. Wang, Y. Feng, L. Yu, and J.-P. Wang, *J. Magn. Magn. Mater.* **380**, 251–254 (2015).
- ²⁰P. I. Nikitin, P. M. Vetoshko, and T. I. Ksenevich, *J. Magn. Magn. Mater.* **311**(1), 445–449 (2007).
- ²¹L. Tu, K. Wu, T. Klein, and J.-P. Wang, *J. Phys. D: Appl. Phys.* **47**(15), 155001 (2014).
- ²²L. Tu, Y. Jing, Y. Li, and J.-P. Wang, *Appl. Phys. Lett.* **98**(21), 213702 (2011).
- ²³See supplementary material at <http://dx.doi.org/10.1063/1.4934743> for system setup, driving field strength, MNP size distribution, and multi-tracer imaging.
- ²⁴S. Biederer, T. Knopp, T. Sattel, K. Lüdtke-Buzug, B. Gleich, J. Weizenecker, J. Borgert, and T. Buzug, *J. Phys. D: Appl. Phys.* **42**(20), 205007 (2009).
- ²⁵J. B. Weaver, A. M. Rauwerdink, C. R. Sullivan, and I. Baker, *Med. Phys.* **35**(5), 1988–1994 (2008).
- ²⁶R. Chantrell, S. Hoon, and B. Tanner, *J. Magn. Magn. Mater.* **38**(2), 133–141 (1983).